

Weierstraß-Institut für Angewandte Analysis und Stochastik

im Forschungsverbund Berlin e.V.

Preprint

ISSN 0946 – 8633

A molecular dynamics view of hysteresis and functional fatigue in martensitic transformations

Oliver Kastner¹, Graeme J. Ackland², Gunther Eggeler¹, Wolf Weiss³

submitted: March 24, 2010

¹ Institute for Materials
Department of Materials Science
Ruhr-University Bochum
44790 Bochum
Germany
E-Mail: oliver.kastner@rub.de
gunther.eggeler@rub.de

² School of Physics
University of Edinburgh
UK
E-Mail: G.J.Ackland@ed.ac.uk

³ Weierstrass Institute
for Applied Analysis and Stochastics
Mohrenstr. 39
10117 Berlin
Germany
E-Mail: wolf.weiss@wias-berlin.de

No. 1497

Berlin 2010



2000 *Mathematics Subject Classification.* 74N15, 70F10, 70E50, 82B26, 74N30.

Key words and phrases. Martensitic transformations, shape memory alloys, solid-solid phase transitions, hysteresis, functional fatigue.

Edited by
Weierstraß-Institut für Angewandte Analysis und Stochastik (WIAS)
Mohrenstraße 39
10117 Berlin
Germany

Fax: + 49 30 2044975
E-Mail: preprint@wias-berlin.de
World Wide Web: <http://www.wias-berlin.de/>

Abstract

Shape memory alloys (SMA) exhibit a number of features which are not easily explained by equilibrium thermodynamics, including hysteresis in the phase transformation and "reverse" shape memory in the high symmetry phase. Processing can change these features: repeated cycling can "train" the reverse shape memory effect, while changing the amount of hysteresis and other functional properties. These effects are likely to be due to creation of persistent localised defects, which are impossible to study using non-atomistic methods. Here we present a molecular dynamics simulation study of this behaviour. To ensure the largest possible system size, we use a two dimensional binary Lennard-Jones model, which represents a reliable qualitative model system for martensite/austenite transformations. The evolution of the defect structure and its excess energy is investigated in simulations of cyclic transformation/ reverse transformation processes with 160,000 atoms. The simulations show that the transformation proceeds by non-diffusive nucleation and growth processes and produces distinct microstructure. Upon transformation, lattice defects are generated which affect subsequent transformations and vary the potential energy landscape of the sample. Some of the defects persist through the transformation, providing nucleation centres for subsequent cycles. Such defects may provide a memory of previous structures, and thereby may be the basis of a reversible shape memory effect.

Contents

1	Hysteresis and functional fatigue in shape memory alloys	3
2	Model material: Binary Lennard-Jones crystals	4
3	Thermodynamics	7
4	Infinite and perfect Lennard-Jones lattices	8
4.1	Harmonic limit: Linearised equations of motion.	8
4.2	Thermodynamic phase stability	9
5	Approaches to hysteresis	13
6	MD simulation experiments of cyclic transformations	13
6.1	Scope	13
6.2	MD simulations	14
6.3	MT in a virgin 160,000 atom quad	14
6.4	Reverse transformation	16
6.5	Cyclic transformation processes	18
7	Hysteresis and functional fatigue in a Lennard-Jones crystal	22
8	Conclusions and Remarks	24
A	Appendix	25
A.1	Quasi-harmonic analysis	25
A.2	Approximation of the partition function	26

1 Hysteresis and functional fatigue in shape memory alloys

Process diagrams of shape memory alloys (SMA) — such as the stress/strain- or the strain/temperature-diagram — are characterised by hysteresis[1]. The width and shape of the hysteresis depend on the specific alloy, its crystal structure, processing parameters or even specific tensile loading directions. Also, hysteresis appears to depend on the history of the processes performed with the material: the transformation stresses and the transformation temperatures change after cyclic mechanical or thermal loading. This effect is most pronounced for virgin materials after casting/heat treatment, but also affects their service properties. Material scientists subsume such behaviour under the terminology *functional fatigue* [2, 3, 4, 5] because of its detrimental effect on material reliability in technical applications.

Hysteresis and functional fatigue in SMA are related to microstructure and its evolution upon thermo-mechanical processes [8, 9]. The characteristic twinned-plate structures of martensite consist of compatible variants formed by accommodation processes during the martensitic transformation (MT) [10, 11]. Since lattice mismatch between the phases inevitably leads to an increased energy at the interface, nucleations typically occur at loci where some pre-existing inhomogeneity offers favourable conditions, for example at grain boundaries, lattice inclusions or surfaces. Additionally, nucleation is influenced by stochastic fluctuations of the field variables. The reverse transformation process from martensite into austenite evolves similarly. This reverse transformation turns out to be accompanied by irreversible lattice variations which can be observed experimentally: Figure 1 shows a TEM micrograph of the same region in a NiTi specimen upon (a) temperature-induced martensitic transformation and (b) after the reverse transformation is completed. Inspection shows the characteristic wedge-shaped martensitic region seen in the forward transformation (a) leaves behind a distinct dislocation mark within the austenite matrix after reverse transformation in (b). Therefore, a transformation/re-transformation cycle introduces microstructural changes and accordingly the energetic situation changes too.

Hysteresis loops in the process diagrams indicate energy dissipation, or entropy production [12]. The thermodynamic phase equilibrium condition based on the free energy implies reversibility and therefore does not include hysteresis a priori. In addition to bulk free energy, continuum models typically introduce interface energies in a phenomenological way. Two classical ideas are used [13]: either the interfaces are considered as singular surfaces with a localised surface energy [14], or the interface is considered as a steep but smooth transition zone and the interface energy is modelled proportionally to the square of the strain gradient [15, 16].

We present studies of the impact of the microstructure on the phase transformation condition by molecular dynamics simulations. This method is in principle the most versatile way of describing solid-solid phase transitions, since the crystal and interfacial structures arise automatically from the inter-atomic potential, as do the long range strain effects; so there is no need for implicit assumptions about microscopic details and symmetry entailed in continuum methods. In particular, thermodynamics emerges from molecular dynamics rather than being an input, so all the fluctuations are incorporated properly. The drawbacks are, firstly, that the model sizes

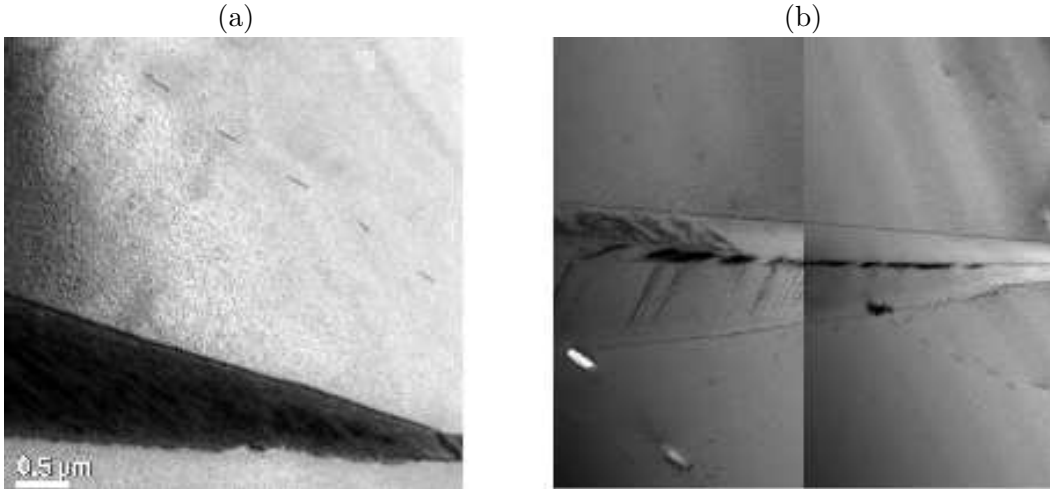


Figure 1: TEM micrograph of the same region in a NiTi specimen upon temperature-induced martensitic transformation (a) and after the reverse transformation (b). The dark region in (a) indicates a T-induced martensite wedge. The wedge leaves faint dislocation marks in (b) after reverse transformation. After [6, 7] with courtesy of the authors.

and the time scales accessible are in the nano-scale due to limited computational resources and secondly, that the models for inter-atomic forces in real materials are still unreliable [17]. In this study, finite size effects are reduced by working in two dimensions, saving computer resource for longer simulation run times and larger systems. The second problem is not solved in this work. Instead we employ a binary Lennard-Jones model which is proven to represent a reliable model system for martensite/austenite transformations. In MT, this model material produces characteristic martensitic microstructures surprisingly similar to real materials [25, 26, 27].

We will describe a series of MD simulations of a cyclic transformation process (see Section 6). A domain structure is formed in our simulations of MT, with domain boundaries containing defects which remain after reverse transformation. These defects change the potential energy landscape of the austenite, and affect subsequent transformations. We will investigate the energetic implications of this defect structure and the consequences of microstructural evolution. Because these processes can be hindered by significant nucleation barriers, the transformations are induced partly by temperature and partly by slow changes of the inter-atomic potential.

2 Model material: Binary Lennard-Jones crystals

We use 2D Lennard-Jones (L-J) crystals in our molecular dynamics simulation experiments [28, 29]. This model material forms binary compounds of two atomic species, A and B, with crystal structures as shown in Figure 2. The model austenite, Figure 2 (a), is represented by nested square sub-lattices of A and B type. In the binary L-J system, the square lattice can be stabilised by temperature or appropriate adjustment of the cross-species (A,B) interactions. The model martensite, Figure 2(b), is produced by a shear/shuffle transformation of the square lattice: square unit cells are sheared into diamonds, accompanied by shuffle of the sub-lattices.

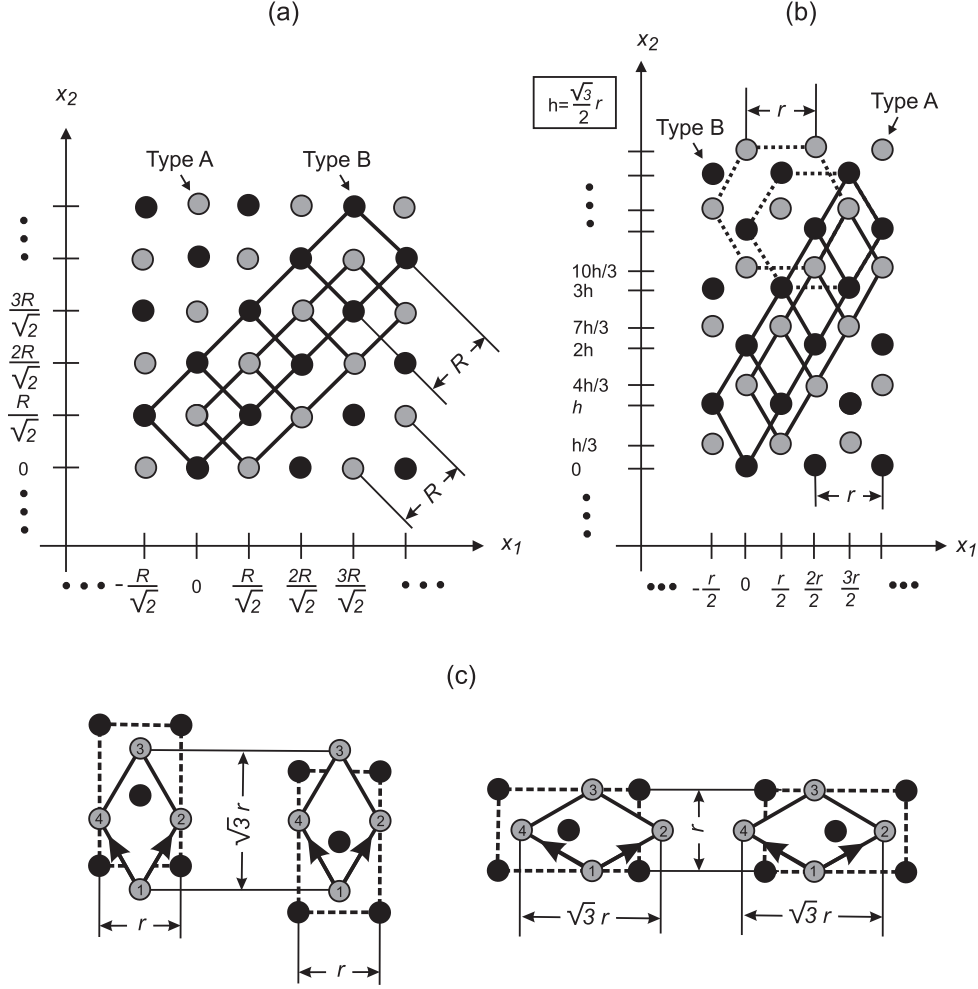


Figure 2: Binary Lennard-Jones lattices in 2D. (a): Model austenite, (b): model martensite, (c): Variants of martensite due to different shear directions of an austenitic unit cell and different shuffle directions of (A,B)-type sub-lattices. Compatible twins have opposite shear but identical shuffle.

Since there are two shear and two shuffle directions possible in 2D, four variants of martensite can be identified, see Figure 2(c). Note there is no group-subgroup relationship between martensite and austenite because the martensite develops a threefold symmetry. This leads to an unusual situation where the atomistic structure is preserved across a compatible variant boundary. Such twin boundaries have zero excess energy and can be located only by reference to the parent austenite.

In molecular dynamics (MD) simulations, the trajectories $\mathbf{x}_\alpha(t)$ of the particles in an N -atom super cell are numerically calculated on basis of the Newtonian equations of motions

$$m_\alpha \ddot{\mathbf{x}}_\alpha = \mathbf{f}_\alpha = - \sum_{\beta \neq \alpha}^N \nabla_\alpha \Phi_{\alpha\beta} \quad (1)$$

with \mathbf{f}_α — the overall interaction force acting on atom α in the presence of the remaining $(N - 1)$ atoms of the system.

In this study, we consider (12,6) Lennard-Jones (L-J) potentials,

$$\Phi_{\alpha\beta}(r_{\alpha\beta}) = 4\epsilon_{\alpha\beta} \left(\left(\frac{\sigma_{\alpha\beta}}{r_{\alpha\beta}} \right)^{12} - \left(\frac{\sigma_{\alpha\beta}}{r_{\alpha\beta}} \right)^6 \right) . \quad (2)$$

$\epsilon_{\alpha\beta}$ and $\sigma_{\alpha\beta}$ are the interaction parameters which depend on the atomic species of atoms α and β . σ determines the potential range while ϵ determines its strength. The distance between atoms α and β is $r_{\alpha\beta} \equiv |\mathbf{x}_\beta - \mathbf{x}_\alpha|$.

In a binary model three potential functions are needed to model interactions between A-A, B-B and A-B atoms, hence there are six interaction parameters $(\epsilon_{AA}, \sigma_{AA})$, $(\epsilon_{BB}, \sigma_{BB})$ and $(\epsilon_{AB}, \sigma_{AB})$. A-A and B-B potentials model bonds between the pure species while the A-B potential defines the cross-species interaction. The balance between pure- and cross-species potentials determines the stability and crystal structure of the binary lattice.

Here we follow [28] in setting interaction parameters of the pure species $(\epsilon_{AA}, \sigma_{AA})$ and $(\epsilon_{BB}, \sigma_{BB})$ to

$$\begin{aligned} \epsilon_{AA} &= 1.2 \epsilon_0 \\ \epsilon_{BB} &= 0.61 \epsilon_0 \\ \sigma_{AA} &= \sigma_{BB} = 2^{-1/6} \sigma_0 . \end{aligned} \quad (3)$$

$\epsilon_{AA} > \epsilon_{BB}$ means that A-A bounds are stronger bound than B-B bounds.

For convenience we use non-dimensionalised quantities and choose $\sigma_0 = 10^{-10}$ m, $\epsilon_0 = 2.5 \times 10^{-19}$ J and $\mu_0 = 58 \times 10^{-27}$ kg respectively to eliminate length, energy, mass and time units from Equations (1) and (2). The natural unit of time $\tau_0 = 4 \times 10^{-14}$ s represents the period of a harmonic oscillation of an atom of mass μ_0 about the minimum of the pair potential with parameters σ_0 and ϵ_0 .

The choices taken in Equation (3) are arbitrary and no attempt is made to fit the pure species potentials to any real metal. A similar model was presented in [28] and basic thermodynamic properties were investigated in [29]. Other similar models have previously been applied, even in 3D [30, 31, 32, 33, 34, 35], but there are serious difficulties with finite size effects and, therefore, boundary conditions. In order to effectively reduce finite size effects, we will concentrate on 2D. This makes it impossible to directly relate our results to any specific material. For example, the lattice defects obtained from the 2D simulations cannot be directly related to any 3D topological defect. However, qualitative explanations of hysteresis and shape memory, as well as continuum and crystallographic theory, can be equally well applied in 2D. It is these more fundamental concepts that we intend to test.

3 Thermodynamics

We briefly review the thermodynamic phase equilibrium condition: the stable phase has minimum free energy, a balance between energy and entropy. For a tensile specimen, as sketched in Fig. 3, a change in internal energy can arise from heat flow and external loading.

$$\frac{dU}{dt} = \dot{Q} + P \frac{dl}{dt} \quad (4)$$

$$\frac{dS}{dt} \leq \frac{\dot{Q}}{T} \quad (5)$$

U denotes the internal energy (potential and kinetic), S the entropy and \dot{Q} the heat exchanged with the thermostat, the latter assumed to act at a homogeneous surface temperature T . Because the processes are slow on the macroscopic time scale, the kinetic energy of the centre of mass may be neglected.

Eliminating the heat flux between Equations (4) and (5) and applying a Legendre transformation the stability criterion reads

$$\frac{d}{dt} (U - TS - Pl) \leq -S \frac{dT}{dt} - l \frac{dP}{dt} \quad (6)$$

Thus in an ensemble with fixed external load P and fixed temperature T the Gibbs free enthalpy $G \equiv U - TS - Pl$ is minimal in equilibrium. This reduces to the Helmholtz free energy $F \equiv U - TS$ for the special case of zero external loads. At the thermodynamic transition temperature and zero load the specific free energies of austenite and martensite are equal,

$$u_{\text{aust}} - Ts_{\text{aust}} = u_{\text{mart}} - Ts_{\text{mart}} \quad (7)$$

The internal energy of N interacting atoms in a 2D lattice is fully determined by the atomic micro-state $(\mathbf{x}_\alpha, \dot{\mathbf{x}}_\alpha)$. Statistical thermodynamics relates the free energy to the partition function Z by

$$F = -k_B T \ln Z \quad (8)$$

where the canonical partition function is represented by a sum over all possible micro-states available,

$$Z = \sum_{\mathbf{x}_{1\dots N}} \sum_{\dot{\mathbf{x}}_{1\dots N}} \exp \left(-\frac{E_{\text{kin}}(\dot{\mathbf{x}}_{1\dots N}) + E_{\text{pot}}(\mathbf{x}_{1\dots N})}{kT} \right) \quad (9)$$

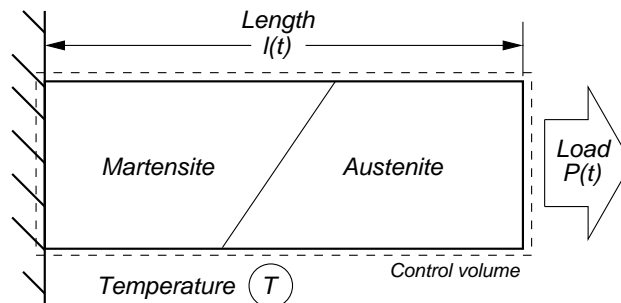


Figure 3: The phase stability criterion. A fixed uni-axially applied load P affects the actual length $l(t)$ doing work at a rate $P dl/dt$.

E_{kin} and E_{pot} are the kinetic and potential energy, given by

$$E_{\text{kin}} = \frac{1}{2} \sum_{\alpha} m_{\alpha} \dot{\mathbf{x}}_{\alpha}^2 \quad (10)$$

$$E_{\text{pot}} = \frac{1}{2} \sum_{\alpha} \sum_{\beta \neq \alpha} \Phi_{\alpha\beta}(|\mathbf{x}_{\beta} - \mathbf{x}_{\alpha}|) \quad . \quad (11)$$

The temperature is related to the mean kinetic energy by

$$e_{\text{kin}}(T) = \frac{E_{\text{kin}}}{N} = k_B T \quad , \quad (12)$$

for N atoms in the 2D case.

For analysis, a useful quantity is the mean ground-state potential energy per atom, e_{pot}^0 i.e. the energy of the system, including defects, at $T=0$. Assuming equipartition, the increase in potential energy at finite T is equal to the increase in kinetic energy. Thus we can estimate:

$$e_{\text{pot}}^0(T) = E_{\text{pot}}(T)/N - k_B T \quad . \quad (13)$$

In the ideal case of infinite and perfect lattices, where surface and lattice defects are absent, this is simply the $T=0$ cohesive energy of the phase in question. The cohesive energy per atom in such a perfect lattice is denoted $e_{\text{pot}}^{0,id}$.

4 Infinite and perfect Lennard-Jones lattices

4.1 Harmonic limit: Linearised equations of motion.

Ideal, static, square or hexagonal lattices are fully defined by the single lattice parameter R or r , respectively, as illustrated in Fig. 2 (a) and (b). For $T \rightarrow 0$ (ground state), these parameters may be determined by potential energy minimisation once the interaction parameters $\{\epsilon_{AA}, \sigma_{AA}, \epsilon_{BB}, \sigma_{BB}, \epsilon_{AB}, \sigma_{AB}\}$ are set. The relaxed lattice sites are denoted by \mathbf{X}_{α}^0 and the displacements from the lattice sites by $u_i^{\alpha}(t) = \mathbf{x}^{\alpha}(t) - \mathbf{X}_{\alpha}^0$. Hence, the linearised equations of motion (1) read

$$m_{\alpha} \ddot{u}_i^{\alpha} = \sum_{\beta} A_{ij}^{\alpha\beta} u_j^{\beta} \quad , \quad (14)$$

where $A_{ij}^{\alpha\beta}(\mathbf{X}_{\gamma}^0)$ is the stiffness matrix. It is determined by the interaction parameters and \mathbf{X}_{α}^0 , see Appendix A.1. Negative eigenvalues of the stiffness matrix imply mechanically stable lattices; this is the *phonon stability criterion*. Martensitic transitions are often associated with phonon instabilities: the eigenvectors coupled with lattice distortions define transformation pathways.

Here, we have fixed the pure-species interactions (Equation 3) and investigate the effect of changing the cross-species interaction parameters ϵ_{AB} and σ_{AB} . Sets of $(\epsilon_{AB}, \sigma_{AB})$ yielding all negative eigenvalues imply a linearly stable lattice, while any positive eigenvalue indicates an unstable lattice. We show these phonon stability limits in the parameter space $(\epsilon_{AB}, \sigma_{AB})$ in Figure 4. It turns out that the stability limits of the two lattices overlap, providing a distinct region in the parameter space where either phase may exist, perhaps metastably, at zero

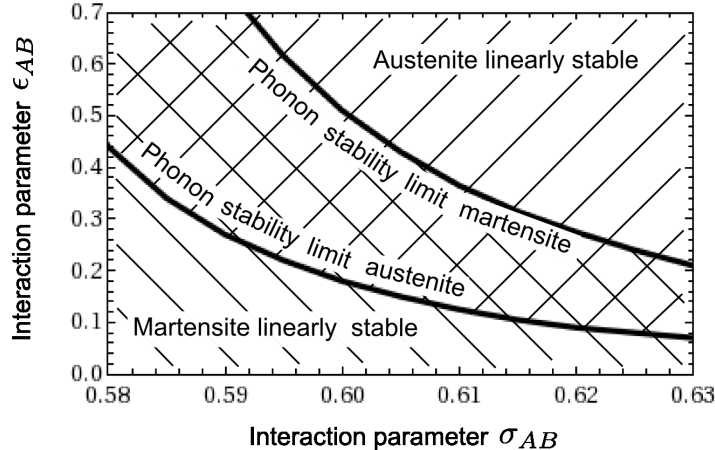


Figure 4: “Phonon stability limits” of square and hexagonal Lennard-Jones lattices in 2D as function of the cross-species interaction parameters ($\epsilon_{AB}, \sigma_{AB}$). Other interaction parameters: $\epsilon_{AA} = 1.2\epsilon_0$, $\epsilon_{BB} = 0.61\epsilon_0$, $\sigma_{AA} = \sigma_{BB} = 0.89\sigma_0$.

temperature. At high temperature, phases which do not satisfy the phonon stability criterion may exist - these are known as *dynamically stabilised*, since this entropic phase stabilisation is a purely dynamic effect which cannot be determined from ground state or harmonic perturbation methods.

The phonon stability criterion can be generalised to finite temperature in the “quasiharmonic” approximation [36], or extended beyond linear theory to treat unstable modes [37], however, it is not equivalent to the thermodynamic phase stability criterion derived in Section 3. Rather, it represents local mechanical stability against small deformations. The thermodynamic phase stability is controlled not by the potential energy alone, but by the free energy, a combination of energy and entropy [38, 39]. Martensite has lower potential energy, while the austenite phase has higher entropy. To study this interplay, and thus produce a set of model parameters which exhibits a martensitic transition, it is necessary to determine energy and entropy independently.

4.2 Thermodynamic phase stability

For infinite and perfect lattices, the free energy ($U-TS$) can be calculated using Equations (8) and (9). There are a number of numerical techniques available [36], but here we adopt an analytic solution obtained under two simplifying assumptions:

1. Einstein crystal: Atoms may be considered to move independently from one another within mean potential energy functions provided by their average environment.
2. Harmonic approximation: Any anisotropies of these mean field potential energies may be neglected in order to represent them as parabolic functions with isotropic curvatures λ .

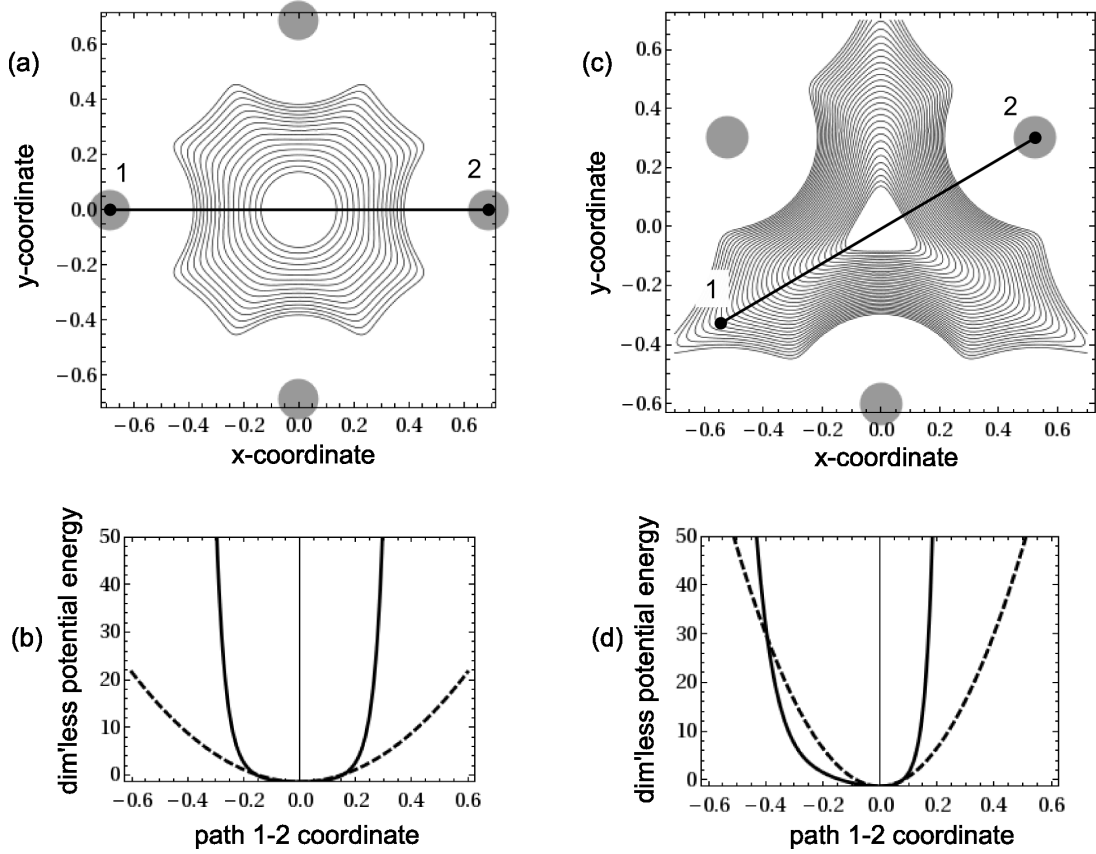


Figure 5: Potential energy of a B-type atom and parabolic approximation. (a), (b): austenite, (c), (d): martensite. One-dimensional representations along the path 1-2 are provided in (b) and (d), where solid lines refer to the anisotropic L-J potential energies and dashed lines to the fitted, parabolic potentials used for the evaluation of the partition function. The situation is similar for A-type atoms.

These two assumptions yield a specific free energy (see Appendix A.2)

$$f_{(\text{aust/mart})} = \underbrace{e_{(\text{aust/mart})}^{0,\text{id}}}_{u_{(\text{aust/mart})}} + k_B T \underbrace{-T k_B \left\{ \ln T + \ln \frac{2\pi k_B T}{\lambda_{\text{aust/mart}}} \right\}}_{s_{\text{aust/mart}}} + C(T) \quad . \quad (15)$$

In this equation terms are sorted so as to emphasise the contributions of the internal energy u and the entropy s to the specific free energy f . Here, $e_{\text{aust/mart}}^{0,\text{id}}$ denote the mean potential energies of an atom located in the ideal lattice and $\lambda_{\text{aust/mart}}$ denote the mean curvatures of their Einstein crystal potentials. $C(T)$ is a constant which contains terms common for both phases austenite and martensite.

The curvatures $\lambda_{A,B}$ of single A- and B-type atoms are fitted to the energy of single-atom displacements in a static lattice averaged over all directions. For illustration, Figure 5 shows equi-potential curves of a single B-type atom inside austenitic and martensitic unit cells. The anisotropic character of the L-J crystal is obvious, but for small amplitudes the approximation of this potential energy by parabolic functions is justified.

Both the ground state energies and the curvatures of the mean potential parabolae are functions of the interaction parameters. In Subsection 4.1 we have pointed out the significance of the cross-species interaction parameters ($\epsilon_{AB}, \sigma_{AB}$) on the lattice stability. In the following we set

$$\sigma_{AB} = 0.60 \quad , \quad (16)$$

hence leaving ϵ_{AB} as the only adjustable model parameter. Figure 6 shows the dependence of $e_{\text{aust/mart}}^{0,\text{id}}$ and the mean curvatures $\lambda_{\text{aust/mart}} = \sqrt{\lambda_A \lambda_B} |_{\text{aust/mart}}$ on this single parameter.

Figure 6 (b) shows that the curvature of the mean potential energy is bigger in martensite than in austenite, $\lambda_{\text{mart}} > \lambda_{\text{aust}}$. Hence, the atoms move in a softer potential in the austenite as compared to the martensite. In fact, the expression $2\pi k_B T / \lambda$ in Equation (15) can be interpreted as the area an atom may explore for a given kinetic energy $k_B T$. Because $\lambda_{\text{mart}} > \lambda_{\text{aust}}$, the austenite has higher entropy than the martensite and thus will be favoured at elevated temperatures. The thermodynamic phase transformation temperature occurs when the free energies of perfect austenite and martensite are equal. This temperature may be calculated approximately from the free energies (15) in the stability condition (7),

$$e_{\text{aust}}^{0,\text{id}} - k_B T_{\text{id}} \ln \frac{2\pi k_B T_{\text{id}}}{\lambda_{\text{aust}}} = e_{\text{mart}}^{0,\text{id}} - k_B T_{\text{id}} \ln \frac{2\pi k_B T_{\text{id}}}{\lambda_{\text{mart}}} \quad . \quad (17)$$

The resulting phase transformation temperature T_{id} for transformations between the ideal lattices is

$$T_{\text{id}} = \frac{e_{\text{aust}}^{0,\text{id}} - e_{\text{mart}}^{0,\text{id}}}{k_B \ln(\lambda_{\text{mart}}/\lambda_{\text{aust}})} \quad . \quad (18)$$

The right-hand-side of this equation depends on the adjustable parameter ϵ_{AB} . Figure 6 (b) shows that the ratio of the curvatures $\lambda_{(\text{aust}, \text{mart})}$ in the denominator is approximately independent of ϵ_{AB} :

$$\frac{\lambda_{\text{mart}}}{\lambda_{\text{aust}}} \approx 2.45 \quad , \quad (19)$$

but the difference of the ground state energies, by contrast, depends significantly on ϵ_{AB} , see Figure 6 (a). Figure 7 shows the dependence of T_{id} on ϵ_{AB} .

T_{id} decreases with ϵ_{AB} monotonically with a root at $\epsilon_{AB} = 0.237$, where the ground state energies of the two phases are identical. Above $\epsilon_{AB} = 0.237$ the material always is austenitic, but MT may be induced by application of external loads [41]. Below $\epsilon_{AB} = 0.237$, martensite has lower potential energy than austenite and here T-induced transformations are possible. Also indicated in Figure 7 is the melting line of the infinite lattice, estimated on the basis of Reference [42]. Its intersection with the transformation temperature line at $\epsilon_{AB} \approx 0.18$ gives a lower bound for the interaction parameter. Note this limit approximately coincides with the phonon stability limit of the austenite: compare to Figure 4 for $\sigma_{AB} = 0.6$. Between the two limits, the transformation temperature depends almost linearly on ϵ_{AB} , while the crystallographies of the model austenite and martensite remain unaffected. MT processes therefore may be induced by change of the temperature at values of ϵ_{AB} within this range (temperature-induced process). Alternatively, they can be induced by variation of ϵ_{AB} at fixed temperature (energy-induced

process). Physically, changing the interactions may be in principle justified to represent changing electronic entropy, which is believed to be significant in the hcp-bcc transition for zirconium [40], or magnetic interactions such as those accompanying the bcc-fcc transition in iron. The main reason we use this technique here is to lower the transformation barrier without changing the character of the two phases. The nucleation rate in MD simulations varies exponentially with the barrier energy, so this is a highly effective way of reducing the necessary computing time. Because changes in ϵ_{AB} do not change the crystallography of the material, the qualitative results and microstructure should be unaffected.

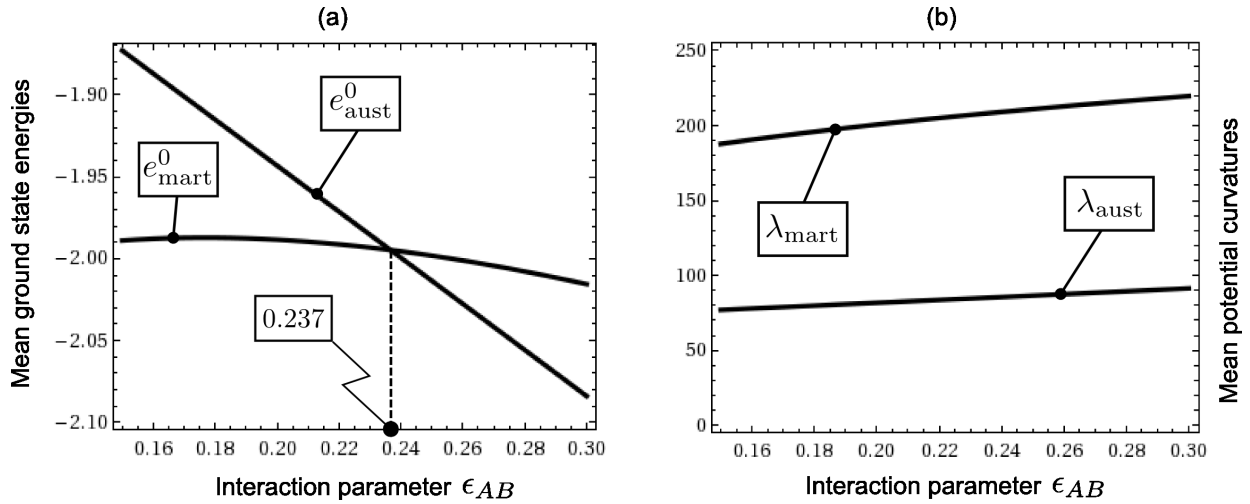


Figure 6: (a): Ground state energies $e_{(\text{aust},\text{mart})}^{0,\text{id}}$, (b): mean curvatures $\lambda_{\text{aust}/\text{mart}} = \sqrt{\lambda_A \lambda_B}|_{(\text{aust},\text{mart})}$ of statically relaxed (austenite, martensite) lattices versus the interaction parameter ϵ_{AB} .

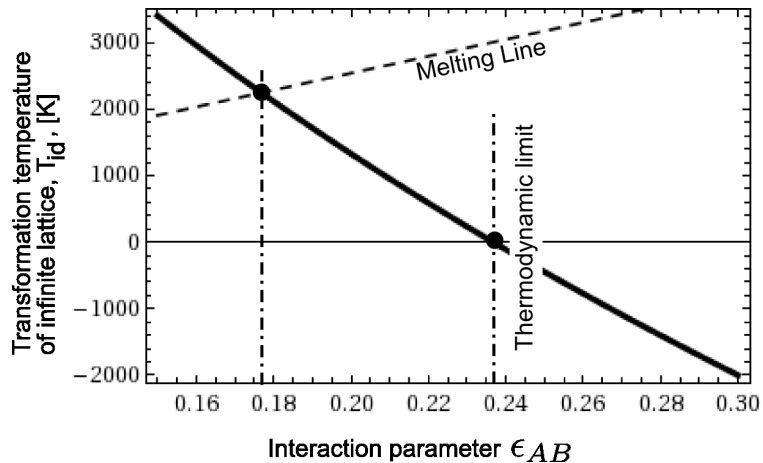


Figure 7: Transformation temperature T_{id} at phase equilibrium of infinite and perfect austenite and martensite lattices as function of the interaction parameter ϵ_{AB} .

5 Approaches to hysteresis

There are two distinct pictures of the cause of hysteresis in a martensitic transformation:

The phonon stability criterion represents the convexity of the atomic potential energy. It is tempting to associate the coexistence range in Figure 4 with the hysteresis [18]. In this picture the transition occurs when the structure is mechanically unstable, and can transform without macroscopic strain. Hysteresis consequently appears as an inherent property of the perfect crystal, independent of any process history.

The other picture relies on the thermodynamic stability condition (6) and relates hysteresis to additional energetic and entropic contributions from defects necessarily created in the transition, and not considered in the theory of perfect and infinite lattices.

The classical nucleation theory for liquid droplets in vapour [19] represents a formulation of the thermodynamic stability criterion, where the additional energy contribution is the interfacial energy between vapour and liquid. The same concept yields hysteresis in condensation/evaporation processes of fluids [20, 21]. Of course, fluid phase theories are simplified by the representation of stresses as isotropic pressure, a single interface energy and the consequence that the nucleus shape is spherical. Solid-solid phase transformations are more complicated, because the phase transformation is affected by *local* compatibility concerns and stress fields to either side of the interface. Further, the interface energy is strongly orientation dependent and affected by defects and dislocations. And finally, the nucleus shape is not known a priori. Continuum models therefore generally simplify solid-solid interfaces as singular surfaces (atomically sharp habit planes and twin boundaries) and assume phenomenological models for the the interface energy. Although an extension of the continuum-level transformation conditions to non-isotropic stresses is available [22, 23, 24], it has not, to our knowledge, yet been applied to the full 3D nucleation problem.

In this second picture, hysteresis arises from local balance equations for some finite control volume, as implied by Section 3. In this case a transformation will only occur once the free energy of the transformed region *including its associated defects* is equal to the untransformed crystal. In what follows, we focus on this concept. We use MD simulations to create microstructure in finite crystals and try to identify its impact on the global thermodynamic phase stability criterion.

6 MD simulation experiments of cyclic transformations

6.1 Scope

In temperature-induced MT, two-dimensional binary L-J crystals produce distinct microstructures which exhibit strong similarities to real materials [25]. The MT evolves by nucleation and growth processes which form herringbone-shaped martensite plates comprising compatible twin variants. Plates growing in perpendicular directions are incompatible, however, and distinct domain boundaries are produced where such plates grow into contact. The incompatibility of

the plates produces lattice defects which we identify by atoms with significantly higher potential energy than those within the martensite plates.

Under reverse transformation, these defects are partly eliminated and partly remain in the lattice where produced. Mobile defects may migrate to the surface where they produce kinks, or they may pile up at obstacles. In any case, the potential energy landscape of the reconstructed austenite is irreversibly changed, and this change influences the subsequent transformations.

To investigate this, a series of transformation cycles were conducted by MD simulation experiments. Because of the significant nucleation barriers, the transformation processes were induced partly by temperature and partly by changing the interaction parameter ϵ_{AB} at constant temperature. Three transformation cycles were conducted, each consisting of five transformation/re-transformation processes. Although starting from slightly different initial conditions, all three cycles show the same morphological and energetic trends and these can be regarded as reproducible.

6.2 MD simulations

Standard NVT MD techniques [43] were employed to integrate the equations of motions of a two-dimensional quad-shaped assembly of 160,000 atoms. The quad has a free surface and no external loads are applied. We use the Verlet algorithm (coordinate formulation) to recursively compute the atomic trajectories with a $\Delta t = 0.4$ fs time-step. The initial atomic velocities were randomly selected and their magnitudes were adjusted to set the required initial temperature. Subsequently, temperature was controlled by use of a Berendsen-type thermostat [44]. In simulations where the phase transformations were induced by temperature changes at fixed ϵ_{AB} (temperature-controlled processes), temperature was changed within a T-interval of $T = 200 \dots 1500$ K at rates of 2 K/fs (0.05 K/time-step). In simulations where the phase transformations were induced by variation of ϵ_{AB} (energy-controlled processes), the temperature was kept constant at either 200 K (for austenite/martensite transitions) or at 1200 K (for martensite/austenite transitions). The interaction parameter ϵ_{AB} then was varied at a rate of $6.25e-7 \epsilon_0/\text{fs}$ within an interval of $\epsilon_{AB} = 0.19 \dots 0.27 \epsilon_0$.

In sum the investigation of the transformation behaviour of the test quad over a T-range of 1300 K and a ϵ_{AB} -range of $0.08 \epsilon_0$ in the three cycles involved a total of ca. 30 million time-steps.

Domain decomposition at cutoff-radii of $r_c = 3.5 \sigma_0$ is used to distribute the computational load over an 8×8 dimensional parallel computing grid, which in the present study was provided by Germany's National Research Centre in Jülich [45] and by a local Beowulf-type Linux cluster.

6.3 MT in a virgin 160,000 atom quad

In the initial state the 160,000 atom quad is a square single-crystal austenite. At a constant temperature of 200 K, martensitic nucleation occurs at $\epsilon_{AB} = 0.19 \epsilon_0$ in this virgin lattice. Primary nuclei typically form at the surface. From here the transformation proceeds into the bulk, forming needle-like martensitic plates of compatible twin variants. A detailed discussion of

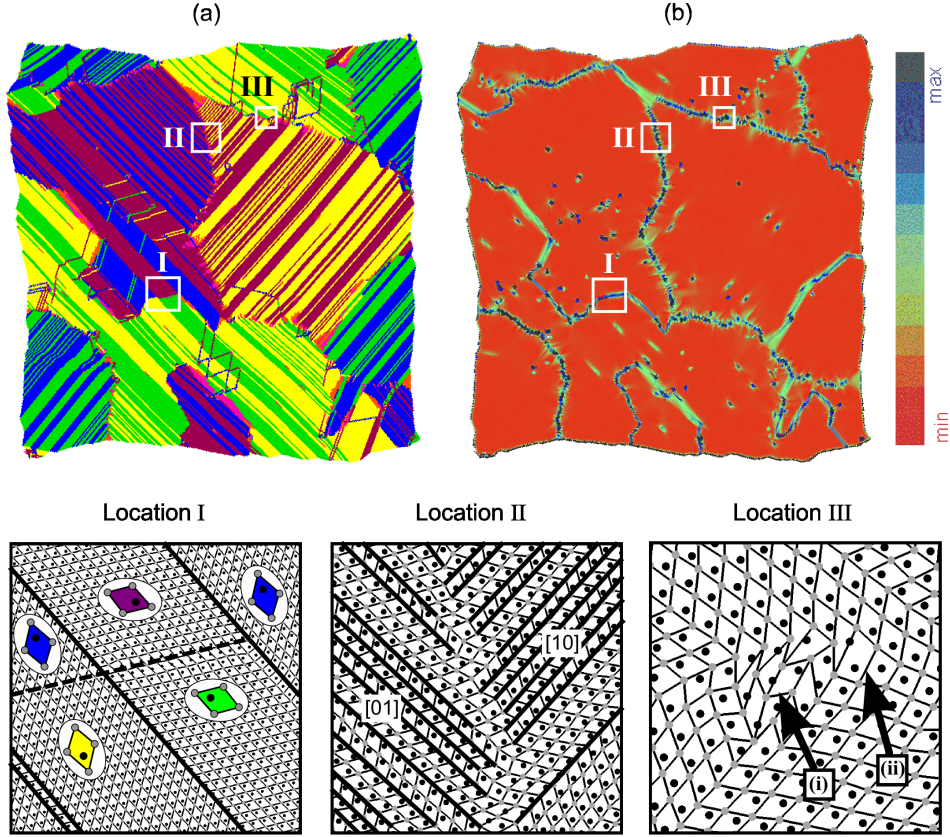


Figure 8: Product of MT in a initially single-crystal 160,000 atom quad. (a): Product morphology. Twins are colour-coded according to the magnification of location I. (b): Potential energy field. Domain boundaries carry higher excess potential energies affecting significant colour contrast. Note that within a single domain, the twin structure visible in (a) is not represented in (b): Twin variants are perfectly compatible and do not exhibit twin/twin interface energy in 2D L-J lattices.

the dynamics of such martensitic nucleation and growth process in 2D L-J crystals is provided in [25]. Here we focus on the product morphology: Figure 8 (a) shows a typical product morphology, and (b) the associated potential energy field. The, martensitic domains consist of finely-twinned microstructures formed by compatible variants (see Figure 2(c)). In the 2D case, L-J twins are perfectly compatible and do not exhibit twin/twin interface energies ¹ and the twinning is identified with reference to the original neighbours of each atom.

Location I in Figure 8 shows the interface between variants with identical shear direction but opposite shuffle directions of the sub-lattices (anti-phase boundary). Such interfaces exhibit significant excess energy along the line where the shuffle changes direction (Figure 8b). Interfaces of this type are typically straight, as indicated by the dotted line in magnification of location I.

Location II in Figure 8 shows the interface between plates which nucleated on the two perpendicular axes [01] and [10] of the austenitic lattice. Variants within each individual plate are compatible, but different plates give rise to misfit at the plate boundaries. The misfit causes

¹This is not the case in 3D!

strain energy, indicated in Figure 8 (b) along boundaries which were produced dynamically where the growing plates come into contact, and thus may have any shape.

At some places along a domain boundary, the incompatibility gives rise to coordination defects. Location III in Figure 8 shows such a situation: the two arrows indicate deformed unit cells at (i) and a vacancy at (ii).

6.4 Reverse transformation

During the reverse transformation, the model material exhibits the two transformation mechanisms sketched in Figure 9, reversible and reconstructive [46]. In reversible transformations nearest neighbour atoms are maintained such that reference austenite unit cells (black lines) keep their shape upon the reverse transformation. In reconstructive transformations the reference unit cells are distorted, as indicated by black lines in the bottom of Figure 9, however, the perfect square lattice is reconstructed locally with the atoms having different neighbours (red lines). The reconstruction produces point defects which either glide to the surface, forming a kink, or pile up at obstacles in the bulk.

Figure 10 illustrates that both mechanisms indeed occur upon reverse transformation of the 160,000 atom block. The top row of this figure shows an austenitic nucleus at low T situated at a martensitic domain boundary marked by reconstructed unit cells and defects at (ii). These defects have excess potential energies shown by the colour contrast in (c). The nucleus mainly consists of reversibly transformed unit cells, but a localised point defect is also visible at (i).

The bottom row in Figure 10 shows the same region after reverse martensite/austenite transformation at high T. The majority of unit cells transformed reversibly into the austenite. Reconstructive transformations have occurred, e.g. in regions (iii) in Figure 10. Colours in 10(b) are assigned with respect to the deformation of reference unit cells defined in the austenite, and hence include historical information. Fig.10(c) shows that the 'reconstructed' region is still perfect austenite with no energy signature. Isolated energetic signatures are observed where the reconstructed region ends (i) and at plate boundary junctions (ii). These defects have both core energy and an associated strain field. Plate boundaries also have increased potential energy, dispersed in a strain field.

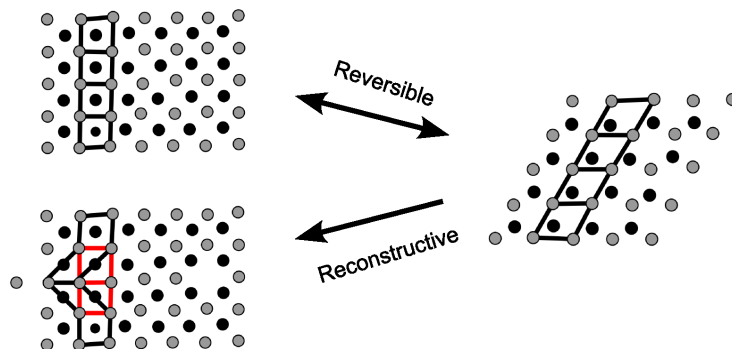


Figure 9: Schematic drawing of two reverse transformation mechanisms.

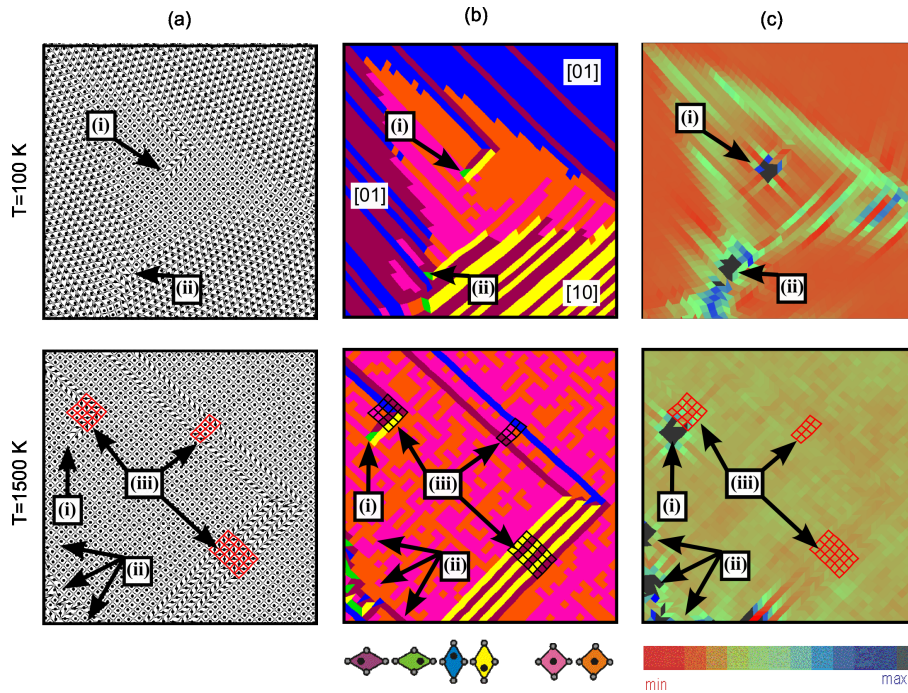


Figure 10: Reverse transformations in the 160,000 atom quad. Top row 100 K, bottom row 1500 K. Columns: (a) lattice, (b) unit cell morphologies, with colours determined from the arrangement of the atoms which were nearest-neighbours in the original austenite (c) potential energy field.

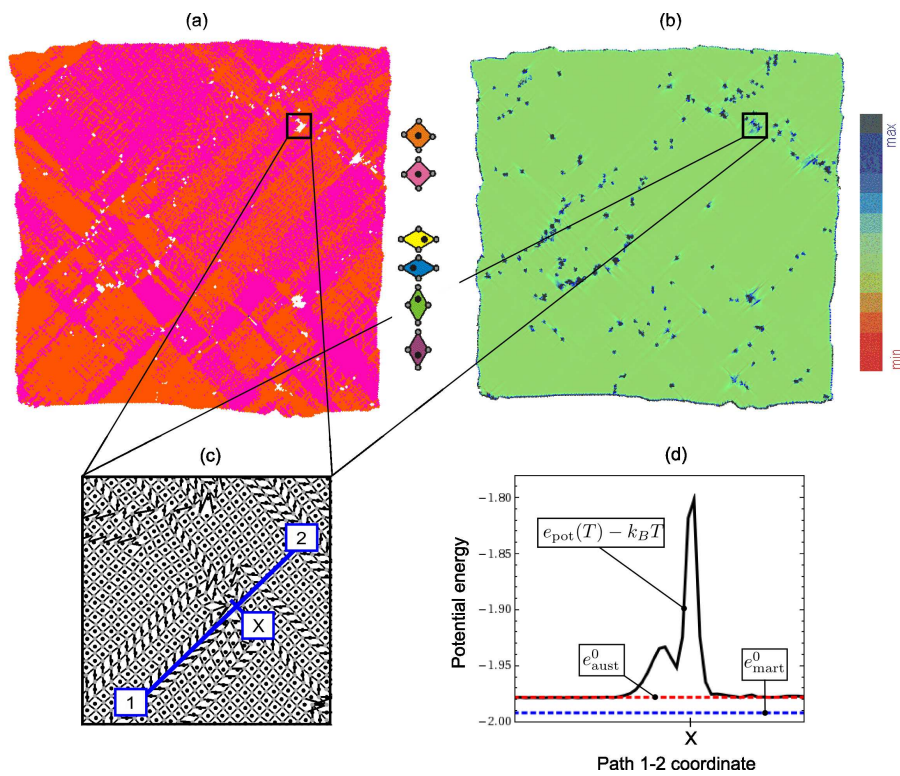


Figure 11: Product of the reverse transformation. (a): Morphology (b): potential energy, (c): magnification of defect region, (d): potential energy across defect along path 1-2.

Figure 11 shows the 160,000 atom quad after completion of the reverse transformation. Frame (a) shows the morphology after re-definition of reconstructed square unit cells as austenite. After this re-definition, some atoms no longer have four nearest neighbours: these are shown as white spots in Figure 11 (a). Inspection of the lattice (c) and the potential energy field (b) shows that these spots represent mostly vacancies, with increased potential energy shown in (d). Away from the spots, the potential energy fluctuates about the energy $e_{(\text{aust,mart})}^{0,\text{id}}$ of the infinite lattice, as indicated by dotted lines in Figure 11 (d).

Martensite has lower potential energy than austenite and the difference is absorbed by the thermostat as latent heat during the transformation.

6.5 Cyclic transformation processes

So far, a single transformation/reverse transformation process was considered. We now consider cyclic transformations, the final configuration of the preceding transformation process being used as the initial configuration of the next cycle. The first transformation cycle with the 160,000 atom quad is initiated from a virgin austenite single crystal. The second cycle is initiated from the product of the first cycle shown in Figure 11.

Figure 12 (a)-(c) show the MT in progress during the second cycle. Martensites nucleate at defects which were produced during the previous transformation cycle. These defects are located along the dotted line indicated in Figure 12 and were preserved during the reverse transformation. Nuclei grow on either side of the defect line, forming differently-oriented martensite plates. And where these new plates interact, new domain boundaries are formed, indicated by (i) in Figure 12 (c).

Thus the defect structure present in the austenite influences the nucleation and growth process of subsequent martensites. This observation is confirmed by further transformation cycles, see Figure 13 for a tableau of morphologies obtained by five subsequent forward/reverse transformation processes with the 160,000 atom quad. The domain character of the martensite is clearly visible in the morphological representation and also by the excess energy of the domain boundaries. Domains are produced during the first MT. Upon reverse transformation, some defects are eliminated, some migrate to the surface. Still others remain immobile during the reverse transformation, and serve as nucleation sites for subsequent MT, hence influencing the new domain structure. This mechanism accounts for an accumulation of defects along lines and eventually imprints a domain structure into the austenite which is reinforced by successive cycles.

The total potential energy of the specimen changes as defects accumulate. Table 1 gives the results of three independent cycle series. Each cycle was started from a perfect, single-crystalline quad. In two series the transformations are induced by slow changes of the interaction parameter ϵ_{AB} at constant temperature, 200 K for MT and 1200 K for its reverse transformation, respectively. The third series was conducted in temperature control mode. To guarantee completion of the transformation processes, the mean potential energy was measured for $\epsilon_{AB} = 0.25 \dots 0.27$

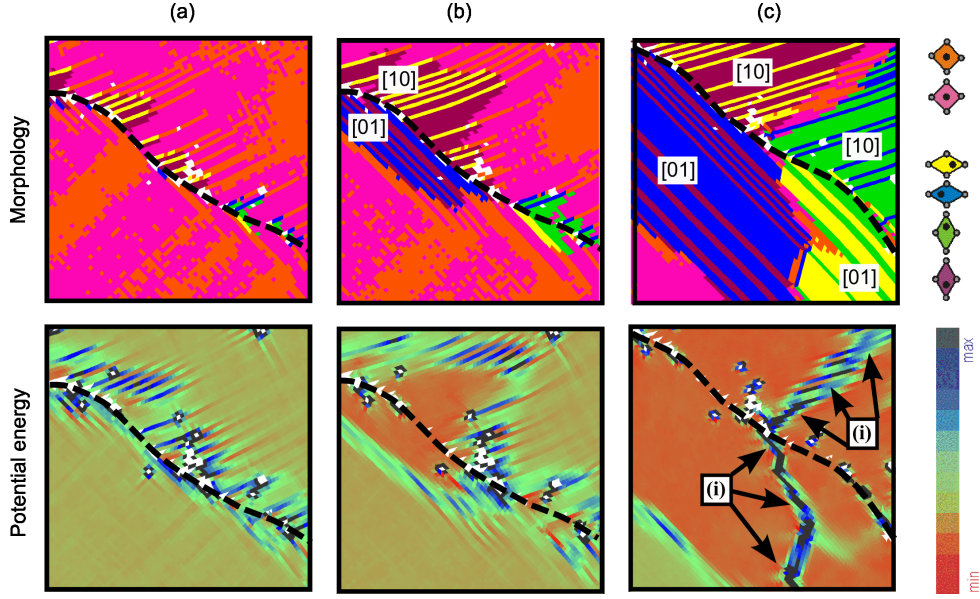


Figure 12: Second transformation cycle: Nucleation of martensite at $T = 200$ K, $\epsilon_{AB} = 0.22$. The dashed line indicates the martensitic domain boundary previously formed.

for reverse transformations and for $\epsilon_{AB} = 0.19$ for MT, respectively. Next, the energies were rescaled to a single, intermediate value of $\epsilon_{AB} = 0.225$ using the constant factors for ideal lattices from Figure 6(a). Finally equation 13 is used to calculate the ground state energies given in Table 1.

Each of the three cycle series produces a different defect morphology, but they exhibit a similar energy trend (Table 1 and Figure 14). The respective ground state energies $e_{(\text{aust, mart})}^{0, \text{id}}$ of the infinite and perfect lattices of Section 4 are also included in Figure 14 by dashed lines. These lines are lower because the pre-transformed samples include the defects and surfaces. The mean excess energies due to defects and surfaces may be defined by

$$\Delta e_{(\text{aust, mart})}^0 = e_{(\text{aust, mart})}^0 - e_{(\text{aust, mart})}^{0, \text{id}} \quad . \quad (20)$$

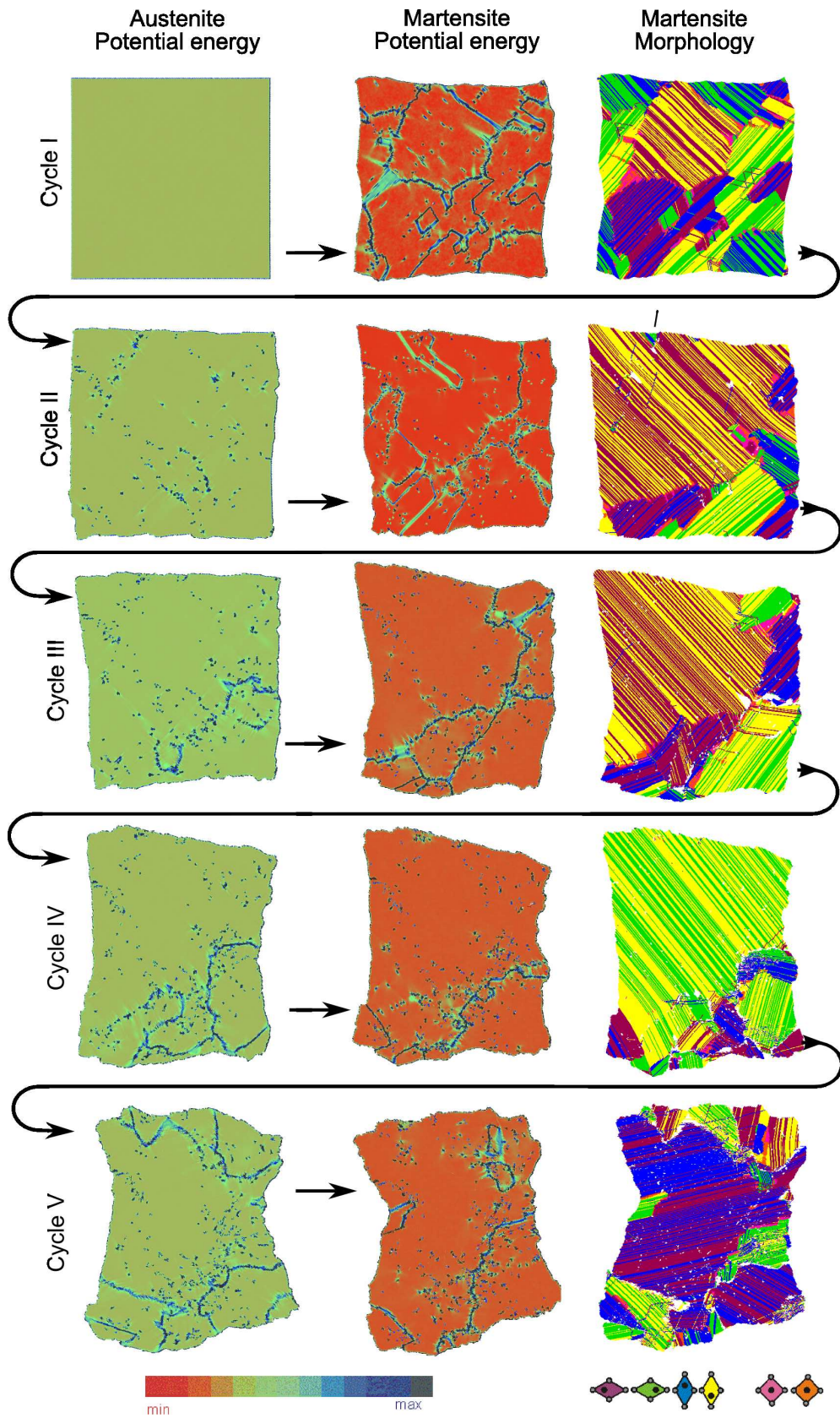


Figure 13: Five cyclic martensitic/austenitic transformations.

Series	AB interaction-parameter	$e_{(\text{aust, mart})}^0$ #cycle				
		I	II	II	IV	V
Austenite, $\times \epsilon_0$						
1	$\epsilon_{AB} = 0.27$	-2.033	-2.031	-2.028	-2.020	-2.015
2	$\epsilon_{AB} = 0.27$	-2.031	-2.025	-2.019	-2.024	-2.023
3	$\epsilon_{AB} = 0.25$	-2.009	-1.999	-1.996	-1.997	-1.994
Trend	$\epsilon_{AB} = 0.225$	-1.969	-1.963	-1.959	-1.958	-1.955
Martensite, $\times \epsilon_0$						
1	$\epsilon_{AB} = 0.19$	-1.970	-1.960	-1.964	-1.966	-1.962
2	$\epsilon_{AB} = 0.19$	-1.959	-1.960	-1.964	-1.974	—
3	$\epsilon_{AB} = 0.19$	-1.975	-1.976	-1.975	-1.977	-1.98
Trend	$\epsilon_{AB} = 0.225$	-1.972	-1.969	-1.971	-1.976	-1.973

Table 1: Estimated ground state energies (U- $k_B T$) measured in three cyclic transformation series with the 160,000 atom quad.

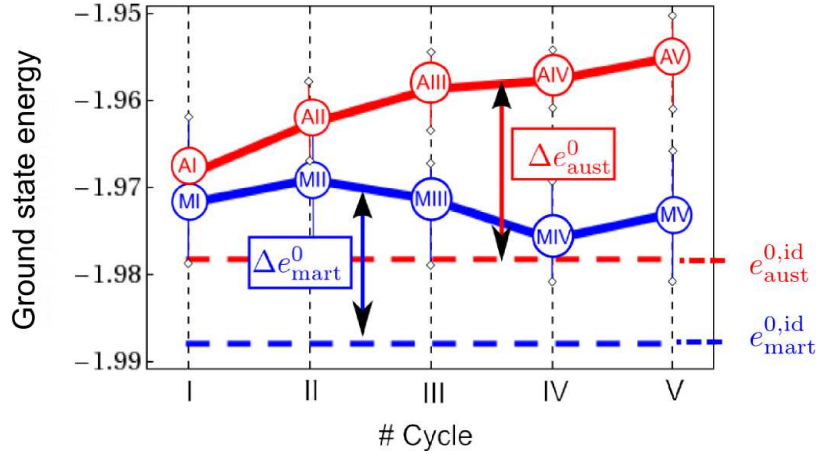


Figure 14: Mean atomic potential energies of the 160,000 quad as a function of the cycle number calculated with $\epsilon_{AB} = 0.225$ using Equation 13. The difference between AI and $e_{\text{aust}}^{0,id}$, shows the contribution from the surface. Solid red and blue curve: Trend lines of austenite and martensite, respectively, according to Table 1. Dashed red and blue lines: Ground state energies of the respective perfect lattices.

7 Hysteresis and functional fatigue in a Lennard-Jones crystal

The results of Table 1 may be interpreted as the cause of hysteresis in the thermodynamic model. The guiding idea is that the excess energies $\Delta e_{(\text{aust, mart})}^0$ shift phase equilibrium condition (17)². For transformation between imperfect structures, the ground state energies in Equation (17) are replaced by the estimated ground state energies of the microstructured lattices, giving

$$T = \underbrace{\frac{e_{\text{aust}}^0 - e_{\text{mart}}^0}{k_B \ln(\lambda_{\text{mart}}/\lambda_{\text{aust}})}}_{T_{\text{id}}} + \underbrace{\frac{\Delta e_{\text{aust}}^0 - \Delta e_{\text{mart}}^0}{k_B \ln(\lambda_{\text{mart}}/\lambda_{\text{aust}})}}_{\Delta T} . \quad (21)$$

Here, ΔT denotes the shift of the transformation temperature due to the defect energies within the microstructure.

Thermodynamic Hysteresis. In the following we consider a sequence of simulations where all transformations were entirely induced by temperature at fixed interaction parameter $\epsilon_{AB} = 0.225 \epsilon_0$. For this case, the potential energies of the defective states are given in Fig 14, indicated by AI...V and MI...V for austenite and martensite, respectively. In the virgin quad the atoms have mean potential energy of AI. Transformation causes a reduction in potential energy to that of the defective martensite. The thermodynamic transformation temperature AI-MI, $T_{AI \rightarrow MI}$, can be calculated from Equation (21) as

$$T_{AI \rightarrow MI} = 59.8 \text{ K} . \quad (22)$$

The reverse transformation goes to defective austenite state AII, which has a higher potential energy than the AI state. The reverse transformation temperature is then higher $T_{MI \rightarrow AII}$

$$T_{MI \rightarrow AII} = 166.8 \text{ K} . \quad (23)$$

Hence, according to thermodynamics, the AI \rightarrow MI \rightarrow AII transformation cycle of the model has a temperature hysteresis of 107 K. Note the transformation temperature T_{id} of the infinite and perfect lattice is above both $T_{AI \rightarrow MI}$ and $T_{MI \rightarrow AII}$ in the first cycle,

$$T_{\text{id}} = 177,0 \text{ K} . \quad (24)$$

Functional fatigue. We need not stop here: going to the next MT of cycle II, the transformation temperature $T_{AII \rightarrow MII}$ depends on the potential energies of states AII and MII and the subsequent reverse transformation by the states MII and AIII. Continuing to the last cycle, the respective transformation temperatures of MT and the reverse transformation are plotted in Figure 15. Inspection shows during the first four cycles both transformation temperatures are increasing beyond the transformation temperature of the infinite lattice T_{id} . The width of the hysteresis decreases during the first four cycles, with some evidence of defect saturation by the fifth cycle. Both transformation temperatures shift upward as a result of the evolution of the defect structure in austenite and martensite.

²we ignore the entropic effect of defects

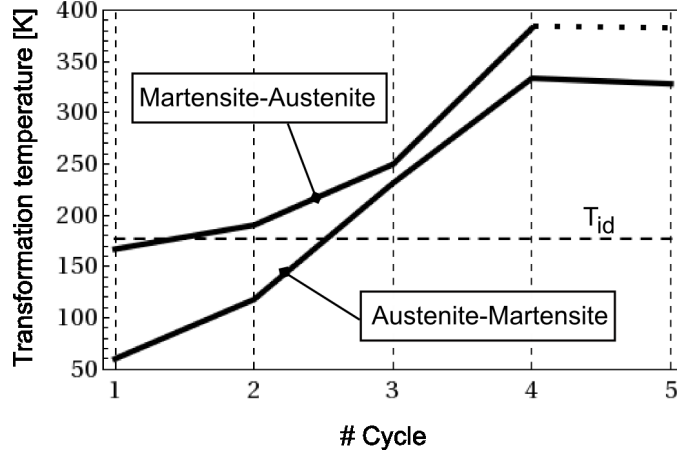


Figure 15: Transformation temperatures of the 160,000 atom quad as function of the cycle number. The hysteresis-free transformation temperature of infinite and perfect lattices (Section 4.2) is indicated by a dashed line.

The cycling was continued beyond the fifth cycle, however, the quad hardens and begins to fracture: necking of the sample is already visible for the last cycles in Figure 13. We regard this as a finite-size effect of the 160,000 atom quad, but larger calculations would have to be compromised by shorter simulation time, i.e. unrealistically fast cooling rates. The chosen assembly size is a compromise in this regard.

Predicted and observed hysteresis. The hysteresis predicted in Figure 15 was based on an integral energy balance of the 160,000 atom crystal. This implies the idea of a homogeneous "mean field" defect energy. Figure 12 in Section 6.5, on the other hand, has illustrated the impact of defects on nucleation, which shows that local conditions are important. The question is whether the local picture of the transformation evolution meets the global prediction?

The answer is "almost". Figure 16 shows the evolution of the austenite fraction of the 160,000 atom quad as function of temperature upon heating and cooling within the range 100..1500 K. Cooling and heating processes were started from identical austenitic and martensitic initial configurations, respectively. These were chosen from previous second-cycle simulations so as to provide defective lattices.

Two different cooling/heating rates were imposed, but the simulations show little difference between the respective curves. Figure 16 shows that the AM transformation occurs quickly upon cooling below 500 K. The MA transformation is sluggish in comparison and remains incomplete for the two chosen temperature rates. The reason for these distinct transformation behaviours is that AM transformations are driven by the potential energy (phonon instability) while MA transformations are driven by the entropy. Entropically controlled transformations involve stochastic processes on the atomic scale and therefore exhibit comparably long relaxation times.

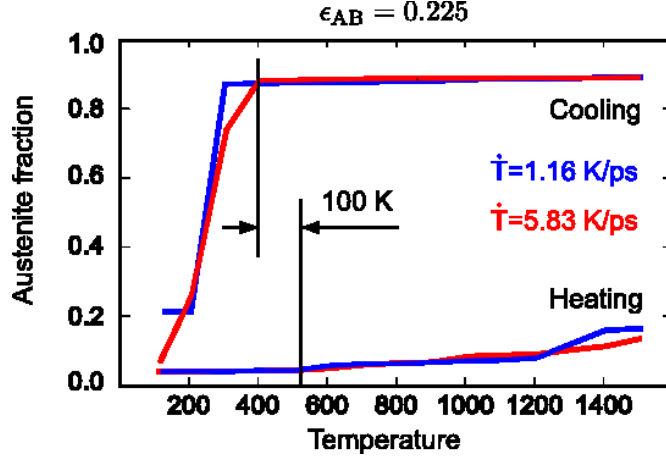


Figure 16: Temperature controlled transformation process of a defect-infected crystal, austenite→martensite upon cooling and martensite→austenite at two distinct temperature rates. For these simulations the cross-species interaction parameter $\epsilon_{AB} = 0.225$ was set constant. Each atom is assigned as austenite, martensite or defective according to how well its local coordination matches the reference structures (Figure 2). As a consequence the defects reduce the maximum austenite fraction below 100%. We associate the MA transition with the first appearance of austenite (“Austenite start”).

The temperature hysteresis for this particular transformation cycle is ca. 100 K, if taken from the first appearance of the product phase (The so-called martensite start and austenite start temperatures). This hysteresis appears to be consistent with the prediction of Figure 15 for a second-cycle transformation with this crystal, however the predicted transformation temperatures do not match.

8 Conclusions and Remarks

The method of MD simulations is capable of modelling microstructure evolutions under MT and the reverse process. In 2D, the size of the test assembly (160,000 atoms) appears to be sufficient to model a domain-structure and its energetic implications. Although the model material is artificial, general ideas about MT should apply equally well to our simulations.

Our simulations exhibit heterogeneous nucleations of martensitic plates comprising compatible twin variants. These plates grow as needles, with the tip moving perpendicular to the habit plane. When martensitic plates encounter one another, the variants are incompatible and the interfaces have high energy. All of this is observed in real MT.

The needle tip, and the joins of boundaries between plates, form point defects which may be identified as 2D analogues of vacancies or dislocations. These defects are not usually eliminated by the reverse transformation, although they may migrate to the surface or pile up in a more extended defective region. There is evidence from TEM that such defects are produced in NiTi.

The simulations show how these defects are introduced during martensitic transformation processes and affect subsequent transformations. If the sample is cycled through a series of forward/reverse transformations, the amount of defects in each phase increases. The defects act as nucleation sources for the transition. Moreover, the location of the defects is preserved through the cycling, providing a memory of previous structures. Eventually, sufficient damage accumulates that the material fractures.

The transformations show pronounced hystereses, and different "start and finish" temperatures. We have developed a thermodynamic theory for the hysteresis, based on the expected defect state of the transformed material. This gives an a posteriori "prediction" for the thermodynamic transition temperature. The MD also gives a transition temperature. This is not sharply defined due to the finite temperature gradient applied, and time lags as latent heat is absorbed by the thermostat. However it is broadly compatible with the thermodynamics prediction.

The thermodynamically-predicted transition temperature increases with cycling, implying that the defect energy in the austenite increases faster than in the martensite. Experiments with SMA show that upon thermal cycling the transformation temperature may indeed increase, but the opposite effect is also observed, depending on the transformation history. However, the nature of the defects observed in 2D may bear little resemblance to those seen in 3D. Furthermore, our thermodynamic condition involves global energies, whereas the transformation is nucleated locally, typically at defects. Further study is required to define and measure the *local* thermodynamic transformation conditions, similar to classical nucleation theory.

In sum, we have used MD to investigate some fundamental principles of cycling martensite/austenite transitions. We show that permanent damage accumulates from plate boundaries in the martensite, which persists through cycling and causes functional fatigue. This damage suggests a natural source for the "memory" and role of "training" in the reverse shape memory effect, and a thermodynamic contribution to hysteresis.

Acknowledgement O. Kastner appreciates funding from the Deutsche Forschungsgemeinschaft (DFG) under contract KA 2304/1,2. The simulations were calculated in parallel on the high-performance facility JUMP located at the NIC [45].

A Appendix

A.1 Quasi-harmonic analysis

The stiffness matrix $A_{ij}^{\alpha\beta}$ is given by

$$A_{ij}^{\alpha\beta} = \frac{\partial f_i^\alpha(\mathbf{X}_\gamma^0)}{x_j^\beta} = \sum_{\nu \neq \alpha} (\delta^{\nu\beta} - \delta^{\alpha\beta}) \left\{ \left(\Phi''_{\nu\alpha} - \frac{\Phi'_{\nu\alpha}}{r_{\nu\alpha}} \right) \frac{r_i^{\nu\alpha} r_j^{\nu\alpha}}{r_{\nu\alpha}^2} + \frac{\Phi'_{\nu\alpha}}{r_{\nu\alpha}} \delta_{ij} \right\}_{\mathbf{X}_\gamma^0} \quad (25)$$

($\delta_{\alpha\gamma}$ and δ_{ij} — Kronecker matrices). The linearised system is solved employing the usual ansatz

$$\mathbf{u}^\alpha(t) = \bar{\mathbf{u}}^\alpha e^{-i\omega t} \quad , \quad (26)$$

(\bar{u}_i^α — complex amplitude, ω — frequency). Hence Equation (14) gives an N -dimensional eigenvalue problem for the eigenvalues $\lambda = -\omega^2$. Since the atomic interactions are short ranged the dimension of this eigenvalue problem may be restricted to the number N_c of atoms located within the cutoff radius about an atom α . We introduce the amplitude vector $\bar{\xi}_I$ and the coefficient matrix $A_{ij}^{\alpha\beta}$,

$$\bar{\xi}_I = \{\bar{u}_x^1 \dots \bar{u}_x^{N_c}, \bar{u}_y^1 \dots \bar{u}_y^{N_c}\}^T, \quad \mathcal{A}_{IJ} = \begin{pmatrix} A_{xx}^{11} & \dots & A_{xx}^{1N_c} & A_{xy}^{11} & \dots & A_{xy}^{1N_c} \\ \vdots & \ddots & \vdots & \vdots & \ddots & \vdots \\ A_{xx}^{N_c 1} & \dots & A_{xx}^{N_c N_c} & A_{xy}^{N_c 1} & \dots & A_{xy}^{N_c N_c} \\ A_{yx}^{11} & \dots & A_{yx}^{1N_c} & A_{yy}^{11} & \dots & A_{yy}^{1N_c} \\ \vdots & \ddots & \vdots & \vdots & \ddots & \vdots \\ A_{yx}^{N_c 1} & \dots & A_{yx}^{N_c N_c} & A_{yy}^{N_c 1} & \dots & A_{yy}^{N_c N_c} \end{pmatrix} \quad (27)$$

and the diagonal mass matrix \mathcal{M}_{IJ} to reduce the eigenvalue problem to the canonical form

$$\sum_{J=1}^{2N_c} (\tilde{\mathcal{A}}_{IJ} - \lambda \delta_{IJ}) \bar{\xi}_J = 0 \quad . \quad (28)$$

Where $\tilde{\mathcal{A}}_{IJ} \equiv \sum_K (\mathcal{M}^{-1})_{IK} \mathcal{A}_{KJ}$ is the dynamical matrix. Equation (28) determines the phonon eigenvalues $\lambda^{(J)}$ and the associated eigenvectors $\bar{\xi}_I^{(J)}$. With $\omega^{(J)} = \pm \sqrt{-\lambda^{(J)}}$ the general solution for the displacements $\xi_I(t) = \{u_x^1 \dots u_x^{N_c}, u_y^1 \dots u_y^{N_c}\}$ reads

$$\xi_I(t) = \sum_{J=1}^{2N_c} \bar{\xi}_I^{(J)} \left(C_1^{(J)} e^{-i\sqrt{-\lambda^{(J)}}t} + C_2^{(J)} e^{+i\sqrt{-\lambda^{(J)}}t} \right) \quad . \quad (29)$$

$C_1^{(J)}$ and $C_2^{(J)}$ are two complex vectors of integration for each mode, which depend upon initial conditions. The phonon stability of the system is readily determined by the eigenvalues: for oscillatory stable solutions the eigenvalues $\lambda^{(J)}$ must be negative.

A.2 Approximation of the partition function

The partition function of Equation (9) can be calculated analytically under the two assumptions of Section 4.2. The first assumption (Einstein crystal) allows us to decouple the energetic states of atoms and the second assumption (paraboloid potentials) allows for analytical integration of the partition function using Gaussian integrals. We use

$$E_{\text{pot}}^\alpha \approx \frac{\lambda_\alpha}{2} (\mathbf{x}_\alpha - \mathbf{X}_\alpha^0)^2 + \varepsilon_\alpha^0 \quad , \quad (30)$$

(\mathbf{X}_α^0 – relaxed lattice positions, λ_α – potential curvature, ε_α^0 – zero-point energy at relaxed lattice position) to simplify the partition function. We obtain

$$\begin{aligned} Z &\approx \prod_{\alpha=1}^N \sum_{\mathbf{x}_\alpha} \sum_{\dot{\mathbf{x}}_\alpha} \exp \left(-\frac{m_\alpha \dot{\mathbf{x}}_\alpha + \lambda_\alpha (\mathbf{x}_\alpha - \mathbf{X}_\alpha^0)^2 + 2\varepsilon_\alpha^0}{2k_B T} \right) = \\ &= \prod_{\alpha=1}^N \frac{1}{Y} \iint_{-\infty}^{\infty} \exp \left(-\frac{m_\alpha \dot{\mathbf{x}}_\alpha + \lambda_\alpha (\mathbf{x}_\alpha - \mathbf{X}_\alpha^0)^2 + 2\varepsilon_\alpha^0}{2k_B T} \right) d\mathbf{x}_\alpha d\dot{\mathbf{x}}_\alpha = \\ &= \prod_{\alpha=1}^N \exp \left(-\frac{\varepsilon_\alpha^0}{k_B T} \right) \frac{4\pi^2 k_B^2 T^2}{Y \lambda_\alpha m_\alpha} \end{aligned} \quad (31)$$

Y is a constant factor taking care of the correct discretisation of the phase space when switching from the quantised to the continuous representation of phase space. With this result the free energy according to Equation (8) reads

$$F = \sum_{\alpha} \varepsilon_{\alpha}^0 - k_B T \ln \prod_{\alpha} \frac{2\pi k_B T^2}{\lambda_{\alpha}} + C'(T) \quad . \quad (32)$$

For infinite and perfect lattices the specific free energy $f = F/N$ is fully determined by two calculations, one for each atom type. For the kinetic energy contribution to the internal energy we add and subtract $k_B T$ and obtain

$$f_{(\text{aust/mart})} = \left[\frac{\varepsilon_A^0 + \varepsilon_B^0}{2} + k_B T - k_B T \left\{ \ln T + \ln \frac{2\pi k_B T}{\sqrt{\lambda_A \lambda_B}} \right\} \right]_{(\text{aust/mart})} + C(T) \quad . \quad (33)$$

Note that in Equation (15) we have used $e_{(\text{aust, mart})}^0 = (\varepsilon_A^0 + \varepsilon_B^0)/2|_{(\text{aust, mart})}$ and $\lambda_{(\text{aust, mart})} = \sqrt{\lambda_A \lambda_B}|_{(\text{aust, mart})}$

References

- [1] K. Otsuka and C.M. Wayman. Shape memory materials. Cambridge: Cambridge University Press, 1998.
- [2] E. Hornbogen. Thermo-mechanical fatigue of shape memory alloys. *J. Mat. Sci.*, 38:1–15, 2003.
- [3] G. Eggeler, E. Hornbogen, A. Yawny, A. Heckmann, and M. Wagner. Structural and functional fatigue of NiTi shape memory alloys. *Mat. Sci. Eng. A*, 378:24–33, 2004.
- [4] E. Hornbogen. Shape memory alloys. In G.J. Bunk, editor, *Advanced Structural and Functional Materials*, pages 133–163. Springer, Heidelberg, 1991.
- [5] E. Hornbogen and G. Eggeler. Surface aspects and fatigue of shape memory alloys (SMAs). *Mat.-wiss. u. Werkstofftech.*, 34:255–259, 2004.
- [6] T. Simon, A. Kröger, A. Dlouhy, and G. Eggeler. In-situ TEM cooling/heating experiments on deformed NiTi shape memory single crystals. In *ESOMAT 2009*. EDP Sciences, 2009.
- [7] T. Simon, A. Kröger, A. Dlouhy, and G. Eggeler. On the multiplication of dislocations during martensitic transformations in NiTi shape memory alloys. *Acta Mat.*, xxxx, 2009.
- [8] H. Sitepu, W.W. Schmahl, J. Khalil-Allafi, G. Eggeler, A. Dlouhy, D.M. Tbbens, and M. Tovar. Neutron diffraction phase analysis during thermal cycling of a Ni-rich NiTi shape memory alloy using the rietveld method. *Scripta Materialia*, 46:543–548, 2002.
- [9] A. Dlouhy, J. Khalil-Allafi, and G. Eggeler. Multiple-step martensitic transformations in Ni-rich NiTi alloys — an in-situ transmission electron microscopy investigation. *Phil. Mag.*, 83:339–363, 2003.

- [10] J.W. Christian. The theory of transformations in metals and alloys. Volumes I, II. Amsterdam and Oxford: Pergamon, Elsevier Science, 2002.
- [11] K. Bhattacharya. Microstructure of martensite. Oxford: Oxford University Press, 2003.
- [12] Y. Huo and I. Müller. Nonequilibrium thermodynamics of pseudoelasticity. *Continuum Mech. Thermodyn.*, 5:163–204, 1993.
- [13] Y. Huo and I. Müller. Interfacial and inhomogeneity penalties in phase transitions. *Continuum Mech. Thermodyn.*, 15:395–407, 2003.
- [14] J.C. Maxwell. *Capillary action*. Encyclopaedia Britannica. 9th edition, 1876.
- [15] J.D. Van der Waals. The thermodynamic theory of capillarity under the hypothesis of a continuous variation of density. *J. Stat. Phys.*, 20(2):200–244, 1979. Translation of the original work from 1893 by J.S. Robinson.
- [16] J.W. Cahn and J.E. Hilliard. Free energy of a nonuniform system, I. interfacial free energy. *J. Chem. Phys.*, 28:258–267, 1958.
- [17] G.J. Ackland, A.P. Jones and R. Noble-Eddy. Molecular dynamics simulations of the martensitic phase transition process. *Materials Science and Engineering A* 481-482, 11 2008
- [18] V.S. Guthikonda and R.S. Elliott. An effective interaction potential model for the shape memory alloy AuCd. *Continuum Mech. Thermodyn.* 21(4):269 – 295, 2009.
- [19] Kelvin (W. Thomson). On the equilibrium of vapour at a curved surface of liquid. *Proc. Roy. Soc. Edinburgh.*, 7, 1872.
- [20] I. Müller. Boiling and condensation with interfacial energy. *Meccanica* 31: 489-494, 1996.
- [21] Y. Huo and I. Müller. Nucleation of Droplets in a Binary Mixture. *Meccanica* 38: 493-504, 2003.
- [22] W. Heidug and F.K. Lehner. Thermodynamics of coherent phase transformations in non-hydrostatically stressed solids. *PAGEOPH* 123, 1985.
- [23] I. Müller. Eshelby tensor and phase equilibrium. *Theor. Appl. Mechanics* 25:77–89, 1999.
- [24] G. Buratti, Y. Huo and I. Müller. Eshelby tensor as tensor of free enthalpy. *J. Elast.* 72(1-3):1–27, 2003.
- [25] O. Kastner and G.J. Ackland. Mesoscale kinetics produces martensitic microstructure. *J. Mech. Phys. Solids*. doi:10.1016/j.jmps.2008.09.016, 2008.
- [26] O. Kastner and G.J. Ackland. Atomistic simulations of martensitic transformations in lennrad-jones solids. part i. In *Science and Supercomputing in Europe*, pages 950–959. HPC-Europa, 2007.

- [27] O. Kastner and G.J. Ackland. Atomistic simulations of martensitic transformations in lennard-jones solids. part ii. In *Science and Supercomputing in Europe*, pages 960–962. HPC-Europa, 2007.
- [28] O. Kastner. Molecular dynamics of a 2d model of the shape memory effect. part I: Model and simulations. *Continuum Mech. Thermodyn.*, 15(5):487–502, 2003.
- [29] O. Kastner. Molecular dynamics of a 2d model of the shape memory effect. part II: Thermodynamics of a small system. *Continuum Mech. Thermodyn.*, 18(1-2):63–81, 2006.
- [30] U. Pinsook and G.J. Ackland. Simulation of martensitic microstructural evolution in zirconium. *Phys. Rev. B*, 58(17):11252, 1 November 1998.
- [31] U. Pinsook and G.J. Ackland. Atomistic simulation of shear in a martensitic twinned microstructure. *Phys. Rev. B*, 62(9):5427–5434, 1 September 2000.
- [32] T. Suzuki and M. Shimono. A simple model for martensitic transformations. *J. Phy. IV France*, 112:129–132, 2003.
- [33] X.D. Ding, T. Suzuki, X.B. Ren, J. Sun, and K. Otsuka. Precursors to stress-induced martensitic transformations and associated superelasticity: Molecular dynamics simulations and an analytical theory. *Physical Review B*, 74, 2006.
- [34] F.E. Hildebrand and R. Abeyaratne. An atomistic investigation of the kinetics of detwinning. *J. Mech. Phys. Solids*, doi:10.1016/j.jmps.2007.09.006, 2007.
- [35] R.S. Elliott, J.A. Shaw, and N. Triantafyllidis. Stability of thermally-induced martensitic transformations in bi-atomic crystals. *J. Mech. Phys. Solids*, 50:2463–2493, 2002.
- [36] G.J.Ackland. Calculation of free energies from ab initio calculation *J.Phys.CM*, 14, 2975 2002.
- [37] N.D.Drummond and G.J.Ackland Ab initio quasiharmonic equations of state for dynamically stabilized soft-mode materials *Phys.Rev.B* 65, 184104 2002.
- [38] O. Kastner. *Zweidimensionale molekular-dynamische Untersuchung des Austenit ↔ Martensit Phasenübergangs in Formgedächtnislegierungen*. PhD thesis, Technical University of Berlin, 2003.
- [39] I. Müller and W. Weiss. *Entropy and energy*. Springer, 2005.
- [40] F. Willaime and C. Massobrio Temperature-induced hcp-bcc phase transformation in zirconium: A lattice and molecular-dynamics study based on an N-body potential *Phys.Rev.Letters*,63, 2244 - 2247 1989.
- [41] O. Kastner and G.J. Ackland. Load-induced martensitic transformations in pseudo-elastic Lennard-Jones crystals. SMASIS08-413 in: *Proceedings of SMASIS08 ASME Conference*

on Smart Materials, Adaptive Structures and Intelligent Systems. October 28-30, 2008, Ellicott City, Maryland, USA.

- [42] E.A. Mastny and J.J. de Pablo. Melting line of the Lennard-Jones system. *J. Chem. Phys.*, 127(104504,), 2007.
- [43] D. Frenkel and B. Smit. *Understanding Molecular Simulation. From Algorithms to Applications.* Academic Press, San Diego (etc.), 1996.
- [44] H.J.C. Berendsen, J.P. M. Postma, W.F. van Gunsteren, A. DiNola, and J.R. Haak. Molecular dynamics with coupling to an external bath. *J. Chem. Phys.*, 81(8):3684–3690, 1984.
- [45] John von Neumann Institute for Computing (NIC), internet resource. <http://www.fz-juelich.de/nic>.
- [46] K. Bhattacharya, S. Conti, G. Zanzotto, and J. Zimmer. Crystal symmetry and the reversibility of martensitic transformations. *Nature Materials*, 428:55–59, 2004.